Anal Bioanal Chem (2011) 401:827–835
DOI 10.1007/s00216-011-5117-x

ORIGINAL PAPER

Detecting small lung tumors in mouse models by refractive-index microradiology

Chia-Chi Chien · Guilin Zhang · Y. Hwu · Ping Liu · Weisheng Yue · Jianqi Sun · Yan Li · Hongjie Xue · Lisa X. Xu · Chang Hai Wang · Nanyow Chen · Chien Hung Lu · Ting-Kuo Lee · Yuh-Cheng Yang · Yen-Ta Lu · Yu-Tai Ching · T. F. Shih · P. C. Yang · J. H. Je · G. Margaritondo

Received: 26 March 2011 / Revised: 10 May 2011 / Accepted: 16 May 2011 / Published online: 30 May 2011

Abstract Refractive-index (phase-contrast) radiology was able to detect lung tumors less than 1 mm in live mice. Significant micromorphology differences were observed in the microradiographs between normal, inflamed, and lung cancer tissues. This was made possible by the high phase contrast and by the fast image taking that reduces the motion blur. The detection of cancer and inflammation areas by phase contrast microradiology and microtomography was validated by bioluminescence and histopathological analysis. The smallest tumor detected is less than 1 mm^3 with accuracy better than 1×10^{-3} mm^3. This level of performance is currently suitable for animal studies, while further developments are required for clinical application.

Keywords Lung cancer · Synchrotron X-ray imaging · Real-time imaging

Introduction

For accurate detection and diagnosis of lung cancer, current imaging techniques include plain radiography, computed

Published in the special issue *Imaging Techniques* (*with Synchrotron Radiation*) with Guest Editor Cyril Petibois.

Electronic supplementary material The online version of this article (doi:10.1007/s00216-011-5117-x) contains supplementary material, which is available to authorized users.

C.-C. Chien · Y. Hwu · C. H. Wang · N. Chen · C. H. Lu · T.-K. Lee
Institute of Physics, Academia Sinica,
Nankang,
Taipei 11529, Taiwan

G. Zhang (✉) · W. Yue · Y. Li · H. Xue
Shanghai Institute of Applied Physics,
Chinese Academy of Sciences,
Shanghai 201800, China
e-mail: zhangguilin@sinap.ac.cn

C.-C. Chien · Y. Hwu
Department of Engineering and System Science,
National Tsing Hua University,
Hsinchu 30013, Taiwan

P. Liu · J. Sun · L. X. Xu
Shanghai Jiao Tong University,
Shanghai 200030, China

Y.-C. Yang · Y.-T. Lu
Mackay Memorial Hospital,
Taipei City 104, Taiwan

Y.-T. Ching
Department of Computer Science,
National Chiao Tung University,
Hsinchu 300, Taiwan

T. F. Shih · P. C. Yang
College of Medicine, National Taiwan University,
Taipei 10617, Taiwan

J. H. Je
X-ray Imaging Center,
Pohang University of Science and Technology Pohang,
Pohang CT, Kyungbuk 790-784, South Korea

G. Margaritondo
Ecole Polytechnique Fédérale de Lausanne (EPFL),
1015 Lausanne, Switzerland

tomography (CT), magnetic resonance imaging (MRI), and positron emission tomography (PET). Among them, the central role of multi-detector CT with contrast administration as a diagnostic and staging tool in the lung cancer is now firmly established [1]. In recent years, a large number of research results were published on low-dose CT screening, with detection rates of early lung cancer varying between 38% and 66% [2].

The detection of small-size lung cancer tumors is particularly important [3, 4] but difficult with the current medical imaging techniques. Contrast based on X-ray absorption can theoretically reveal tumors of diameter down to ≈2 mm [5]. However, most of the stage I lung cancer tumors imaged by CT have a mean size of 15 mm, and the smallest identified tumor size is 1 mm [6, 7] with a high false positive rate [8, 9]. Other imaging techniques are also affected by significant limitations [10]. For example, MRI offers better soft tissue contrast, multiplanar imaging, and other advantages, but is slower and with worse spatial resolution (~3 mm [11]) than CT. PET is able to distinguish between benign and malignant tumors if the size exceeds ~10 mm [12] with spatial resolution ~6 mm [13]. Therefore, histopathology examination of resected specimens is often necessary to distinguish between benign tumors, malignant tumors, and inflamed tissues. For applications confined to animal studies, some more other imaging techniques are available, e.g., fluorescence molecular tomography, but these are also affected by limitations, in particular concerning the resolution.

We present here results on the in vivo detection of millimeter-size cancer tumors in mouse models with refractive-index microradiology using spatially coherent synchrotron X-rays. The tests included not only the discrimination between normal and cancer lung tissues but also between cancer and inflammation. The phase mechanism results both in high contrast and in fast image taking that reduces the effects of motion blur.

Phase contrast enables highly coherent X-rays to produce images with enhanced edges between different specimen regions [14]. Areas with dissimilar (real) refractive index values cause different deviations of the X-ray beam [15]. This produces typical white-dark “fringes” in the radiographs that enhance the visibility of the corresponding boundaries. Added to the standard absorption contrast, the edge enhancement improves the image quality without requiring high radiation doses [16]. Note that absorption-based synchrotron imaging was already applied for clinical tests in angiography [17, 18], and phase contrast was exploited to enhance the effectiveness of the tests for mammography [19, 20].

Phase contrast was also used [21, 22] for lung analysis in animal models and specifically for the detection of cancer tumors [23] with size of several millimeters. In this study, we push the detection to millimeter-size tumors and beyond. This was made possible by improving the contrast, which is in fact the limiting factor in the detection—whereas spatial resolution is actually at the submicron level [24]. The high contrast enabled us to also implement automated tumor and inflammation detection with an image analysis algorithm. This detection technique was tested for in vivo mice radiographs and also for simulated human lung cancer images.

One point emerging from our tests is that refractive-index contrast is particularly suitable for lung tissue analysis compared to other organs and tissues. The lungs consist indeed of many alveoli full of air, and there is a large difference in the refractive index between air, the alveolar walls, and solid tumors.

Materials and methods

The experiments were performed on the BL-01A beamline of the National Synchrotron Radiation Research Center (NSRRC, Hsinchu, Taiwan) and on the 7B2 beamline of the Pohang Light Source (PAL, Pohang, Korea). At NSRRC, unmonochromatized X-rays emitted by a 4.5-tesla superconducting wavelength shifter on the 1.5-GeV electron storage ring crossed two beryllium windows before reaching the object. The beam spot size was 3.23×3.23 mm^2 for live specimens [25]. At PAL, we used unmonochromatized radiation emitted by a bending magnet on the 2.5-GeV storage ring [26].

Details of the image acquisition method were identical to those described in references [14] and [27]. The object–detector distance, ~250–300 mm, was optimized to enhance refraction-contrast effects as discussed in reference [28]. The detector was a Diagnostic Instruments SPOT-RT CCD camera with a $CdWO_4$ single crystal scintillator. The photon flux density was 4.4×10^{12} photons s^{-1} mrad^{-1} (0.1% bandwidth)$^{-1}$(200 mA)$^{-1}$ at the critical photon energy. The beam divergence is 48 μrad and 20 μrad in the horizontal and vertical directions. The estimated vertical coherence length at the critical photon energy is of the order of 700 μm.

A first set of tests was performed at PAL on pathology specimens to show that phase contrast can indeed reveal tumors and inflammations in mice lungs. Then, in vivo experiments were conducted at NSRRC.

The pathology specimens were prepared in the Animal Laboratory of the Shanghai Jiaotong University. *BALB/c* nude mice (20±2 g, 5 weeks old) were acquired from the Animal Center of the Chinese Academy of Sciences (CAS). Another mouse strain, *BALB/cByJNarl* mice (16–21 g, 5 weeks), acquired from the National Laboratory Animal Center, Taiwan, was used for in vivo tests.

Two different cancer cell lines were used: Lewis lung cancer cells were cultured in RPMI-1640 medium with 10% fetal bovine serum, whereas EMT-6 cells were cultured in DMEM/F12 medium. The cells were grown in a 5% CO_2 incubator until they were 90% confluent.

Lewis lung cancer cells $1–2\times10^6$ cells $ml^{-1}\cdot0.1$ ml were surgically transplanted into *BALB/c nude* mice, and EMT-6 cancer cells 1×10^8 cells $ml^{-1}\cdot0.01$ ml were surgically transplanted into the right lobes of lung in *BALB/cByJNarl* mice by the percutaneous inoculation method [29]. Bioluminescence tests on live mice (Electronic Supplementary Material Fig. S1) demonstrated that within 7 days after inoculation, individual pulmonary nodules were developed. For pathology specimens, these nodules were excised from nude mice at different times after implantation and fixed with 10% buffered formalin. The specimens were then cut in 2-mm-thick sections for synchrotron microradiology analysis.

In the case of in vivo tests, we used *BALB/c SI c-nu/nu* (16–21 g, 5 weeks) implanted with Lewis lung cancer cells and *BALB/cByJNarl* mice with EMT-6 cells. The final cancer images for the two lines were similar, but EMT-6 cells grew faster into detectable tumors in *BALB/cByJNarl* mice. Eleven days after Lewis cell implantation and 4–7 days after EMT-6 implantation, the live mice were analyzed by synchrotron microradiology. After such tests, 5-μm-thick histological sections were prepared and stained with hematoxylin and eosin and investigated by transmission optical microscopy using a ×100 oil objective.

The pathology and live specimens for inflammation studies were prepared as follows. *BALB/c nude* mice (20±2 g) were treated as above except that a 0.1-ml $PM_{2.5}$ aerosol particle (from a car tunnel) solution with 14 mg/ml concentration was transplanted into the mice by percutaneous inoculation. Within 3 days from inoculation, hemorrhage occurred, and many erythrocytes accumulated in the lungs.

Twenty-two *BALB/c* SI c-nu/nu nude mice were used for synchrotron imaging: 12 for cancer tests, nine for inflammation tests, and one for control. Forty-two *BALB/cByJNarl* mice implanted with EMT-6 were used for cancer tests. Twenty-four of these were radiographically analyzed in vivo 7 days after the inoculation: ~2 mm tumors were detected in 19 cases and no tumors in the remaining five. The other 18 *BALB/cByJNarl* mice were imaged 4 days after inoculation; ~1 mm tumors were found in 14 mice and no tumors in the remaining four. In addition, four *BALB/cByJNarl* mice were used for bioluminescence imaging that revealed cancer tumors in all of them.

The detection of cancer tumors by synchrotron imaging was systematically cross-checked by histopathology analysis. The results were 100% positive: each case of cancer detection by synchrotron radiology was confirmed by histopathology, and all negative cases for one technique were also negative for the other.

One important issue is of course the X-ray dose. The image taking time for each radiograph (3.8×3.8 mm^2 for live specimens, smaller for pathology objects) was 1–3 ms. For a single exposure, this corresponds to a ~5-Gy dose.

Such a dose is much higher than the levels tolerable for clinical applications. Our tests are of course very far from clinical radiology; however, high doses could be a problem even for animal applications. Note, however, that there is still ample margin to optimize the procedure and drastically reduce the dose, by relaxing the spatial resolution (~1 μm) and using more sensitive detectors such as films. From the experience of other clinical synchrotron tests [16–20], we estimate that the dose could be decreased by a factor $>10^3$.

In addition to projection radiography in vivo, tests on tomography reconstruction were performed on lung specimens removed from sacrificed mice and fixed by paraformaldehyde 4% and postfixed by a 1 wt.% OsO_4 solution for 36 h. Before dehydration, the lungs were washed three times with a large volume of PBS. The specimens were dehydrated with a sequence of ethanol exposures with increasing concentrations up to 100%. The specimens were then dried by a critical point dryer.

Projection images for tomography reconstruction were taken with a 1.65-mm-thick silicon wafer before the specimen to attenuate the X-ray beam. The sample-to-detector distance was 5 cm, and the exposure time was 0.3–0.5 s. For each tomography reconstruction, 1,000 projection images were taken in 10 min with a ×2 lens by rotating the specimen over 180°.

Results and discussion

Pathology specimens

A typical 3.0×3.6-mm^2 patchwork microradiograph of a 2-mm-thick pathology specimen of a mouse lung tumor is shown in Electronic Supplementary Material (Fig. S2). This is representative of a set of five consistent tests on different nude mice. A 0.8-mm dark-grey area (marked by an arrow) is observed, and the subsequent histopathology analysis confirmed that this was a malignant tumor.

The tumor appears in Electronic Supplementary Material Fig. S2A as a single nodule markedly different from the surrounding tissue. The alveolar structure appears destroyed in the tumor area, indicating that the region no longer contains air. In the surrounding region, the structure of the alveoli is still visible.

For comparison, a patchwork image taken on normal tissue (no inoculation) is shown in Electronic Supplementary Material Fig. S2B. Individual alveoli (arrow “a”) and

bronchi (arrow "b") can be detected. In essence, the comparison of Electronic Supplementary Material Fig. S2A, B (as well as of the four other image pairs) shows that millimeter-size (or smaller) lung tumors could be identified with phase contrast.

Figure S2C in the Electronic Supplementary Material shows a patchwork image of tissue affected by pulmonary inflammation; this image is consistent with five more obtained for different mice. Many hemorrhages (e.g., arrow "c") are visible, and the corresponding alveolus structures are denser than in normal tissues. This corresponds to an early stage of lung injury [30–32].

The comparison of images like Fig. S2A, C in the Electronic Supplementary Material reveals the different local morphology of cancer and inflammation specimens. Even without staining, this makes it possible to distinguish between the two pathologies by visual inspection.

Live specimens

Before starting these experiments, we tested the effectiveness of the inoculation method in producing cancer by daily bioluminescence imaging analysis of four mice (Electronic Supplementary Material Fig. S1). The results confirmed that the inoculation induced malignant tumors.

Figure 1a shows a patchwork of microradiology images taken from the chest of a live *BALB/cByJNarl* mouse 7 days after EMT-6 cell inoculation. The circle in Fig. 1a marks the area at the inoculation site where a tumor developed. The tumor is visible in the magnified image of Fig. 1b where its edge is marked by arrows. The shape is outlined by the edge enhancement produced by phase contrast.

Immediately after the radiology test, the mouse was dissected, and a tumor was visually observed at the same place. A subsequent histopathology analysis confirmed the cancer nature of the tumor (Electronic Supplementary Material Fig. S3).

The results of Fig. 1a, b are representative of consistent findings for the ten Lewis cell-implanted nude mice and 22 EMT-6-implanted *BALB/cByJNarl* mice that developed tumors 11 and 7 days after implantation. In each case, tumor features were observed in the phase-contrast images (Electronic Supplementary Material Fig. S4) and confirmed to be cancer areas by histopathology.

To assess the minimum size of cancer tumors detectable in vivo by our approach, we performed tests on the 18 *BALB/cByJNarl* mice 4 days after EMT-6 cell inoculation. A tumor smaller than 1 mm can be observed in Fig. 1c, d. Tumors of millimeter and submillimeter size were actually detected in ten of the 18 mice used for these tests; for the other eight, neither phase contrast radiology not histopathology analysis detected any tumor.

Figure 2 summarizes the results on the phase-contrast radiology determination of the tumor size. The histogram

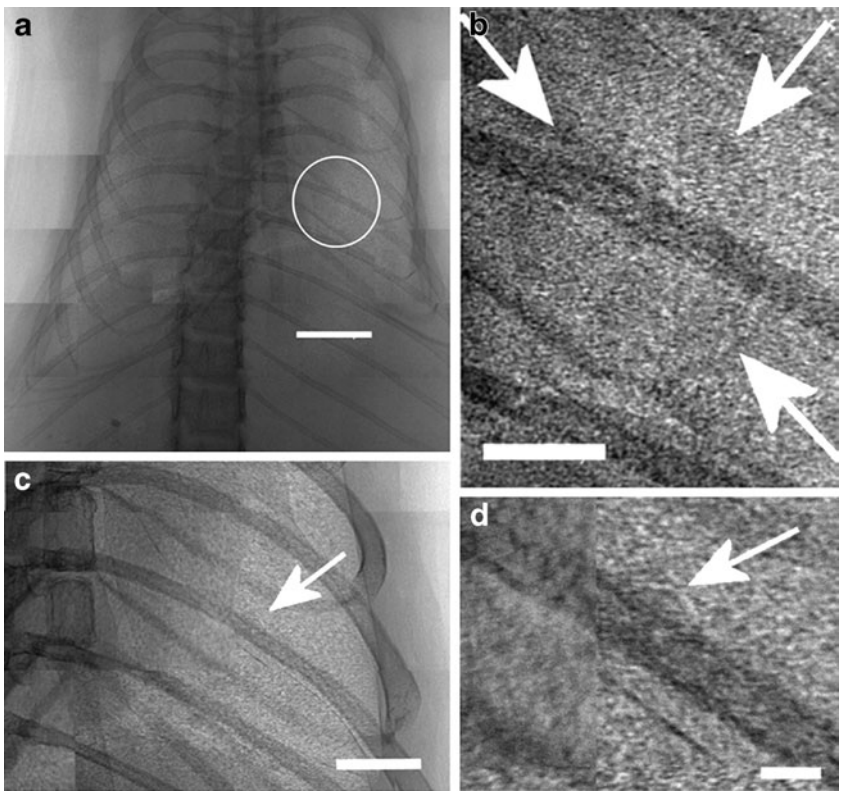

Fig. 1 (**a**) Patchwork of images of the chest of a *BALB/cByJNarl* mouse 7 days after EMT-6 cell inoculation. The *circle* marks a 2-mm spot revealing a cancer tumor; *bar*: 2 mm. (**b**) Zoomed portion of the same picture showing the boundary of the tumor; *bar*: 1 mm. (**c**) Similar in vivo image taken 4 days after inoculation with EMT-6 cells. (**d**) Zoomed portion of the same picture. The *circle* marks a submillimeter cancer tumor. The *bars* are 1 mm in (**c**) and 0.5 mm in (**d**)

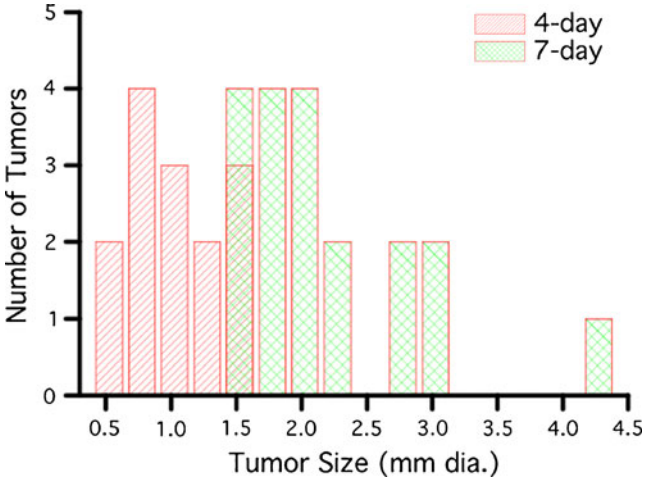

Fig. 2 Histogram showing the distribution of cancer tumor sizes derived from phase-contrast radiology images for EMT-6-implanted *BALB/cByJNarl* mice. The *two colors* identify the distributions are obtained 4 and 7 days after implantation

refers to measurement on the 33 EMT-6-implanted *BALB/cByJNarl* mice that developed tumors 4 or 7 days after implantation. The size distributions for the two waiting times are different: the average size is 1.0 mm in the first case and 2.2 mm in the second. The spread of values is also different, by the overlap between the two distributions is minimal. The main message of Fig. 2 is that phase contrast can lead not only to tumor detection down to the millimeter range but also to accurate and reliable evaluations of the corresponding tumor sizes.

Some of the pathology specimens obtained from EMT-6-inoculated *BALB/cByJNarl* mice 7 days after inoculation (and after in vivo radiology tests) were used to test tumor detection by three-dimensional tomography reconstruction. Results like those of Fig. 3 are representative of four consistent tests of this kind on large tumors. Specifically, Fig. 3a and d are projection radiology images of a cancer area and of a normal area. Figure 3b, e are tomographic reconstructed images for the same areas. The ellipses in Fig. 3a, b mark the tumor area: Fig. 3b reveals in this area a dense tissue structure without bronchi and alveoli—that are instead visible in the normal tissue of Fig. 3e. The photographic image of Fig. 3c shows a tumor in the right lobe, marked by the arrow. From the analysis of the tomographically reconstructed data, we can determine the tumor volume in three dimensions with an accuracy ~1×10^{-3} mm^3 for tumors as small as 1 mm^3. This approach, therefore, provides highly accurate estimates of the tumor size.

The live mice tests included discrimination between cancer and inflammation areas. Figure 4a shows a patchwork of images for a nude mouse 3 days after $PM_{2.5}$ solution inoculation. The magnified image of Fig. 4b zooms on the inoculation area, outlined by the arrows. Faint lines are visible remnants of the alveoli structure, whereas such features were not observed for cancer areas (Fig. 1a, b). *BALB/c* nude mice were purposely used for these inflammation tests to guarantee that the faint lines were not produced by hairs. The histopathology analysis revealed that the inflammation area of Fig. 4b was full of hemorrhages surrounded by inflamed cells.

Image optimization

In addition to the simple visual inspection of the phase contrast images, we tested computer image processing to automatically detect small cancer or inflammation areas and trace their boundaries. Figure 5a, b show the results for the images of Figs. 1a and 4b. The analysis procedure consists of a sequence of steps including mean filtering to remove noise, use of the

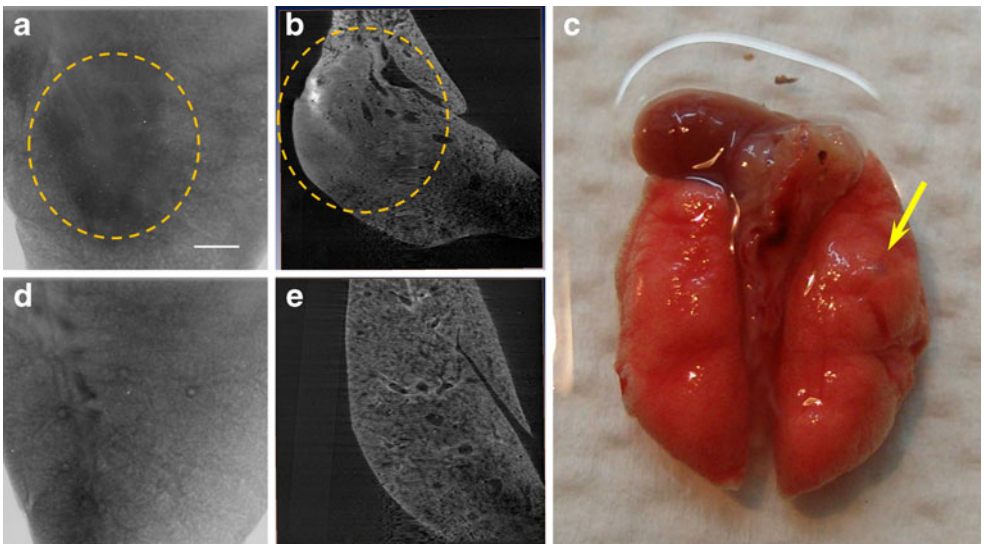

Fig. 3 Tests of tomographic reconstruction: (**a**–**c**) Refer to the lung of a cancer-bearing mouse and (**d**, **e**) to a normal lung; (**a**, **d**) are projection radiographs, whereas (**b**, **e**) are tomographically reconstructed images. A solid tumor in the cranial lobe is marked by *ellipses* in (**a**, **b**) and by an *arrow* in the photographic image (**c**); bar: 0.5 mm

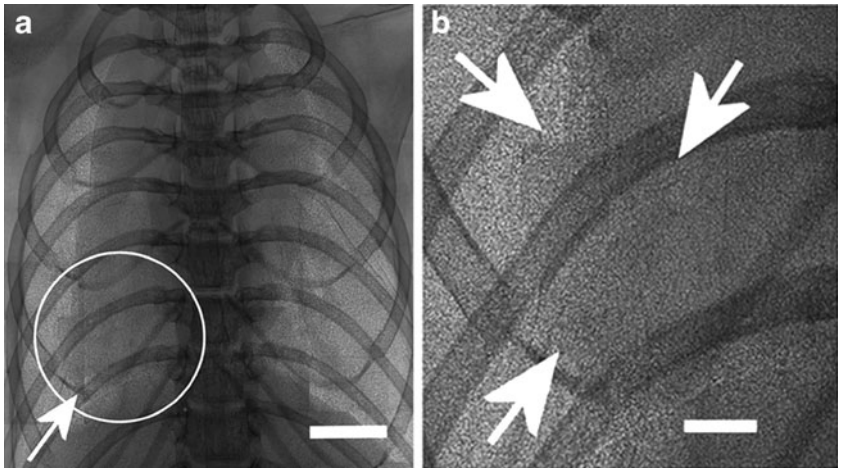

Fig. 4 (**a**) Patchwork image of the chest of a live nude mouse 3 days after $PM_{2.5}$ solution inoculation. The *marked area* correspond to an inflamed region; *bar*: 2 mm. (**b**) Magnified portion of the previous image showing the edge of the inflamed region; *bar*: 0.5 mm

Canny edge algorithm [33] to enhance the boundaries and the gradient vector flow (GVF) [34] snake (active contour) method [35] to segment the region of interest.

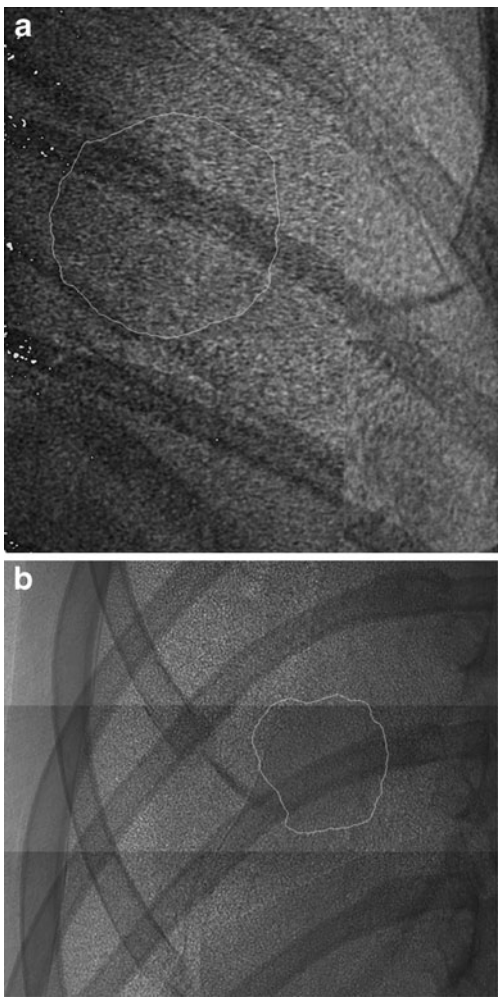

Fig. 5 Image processing partially based on the "gradient vector flow" algorithm identifies tumor or inflammation area boundaries in the microradiographs of Figs. 1a and 4b

We extended this computer method to human-like images in order to tests its feasibility for phase contrast radiology beyond mice. A theoretical model similar to reference [36] was applied with pulmonary alveolus structure data extracted from pathology analysis, to simulate the search for cancer tumors in a human lung. The normal pulmonary alveoli were modeled as spheres with inner and outer radii of 25 and 30 μm and with a random uniform distribution. The simulated sample size was 4.4 mm×4.4 mm×2 cm, and the X-ray was assumed to propagate along the 2-cm direction. A 1-mm size tumor was simulated in the middle of the specimen with spheres having inner and outer radii of 4 and 15 μm. For the index of refraction of the tissue, we used a real part $\delta=2.205\times10^{-7}$ ($\delta=n-1$) and an imaginary part $\mu=12.583\ \mathrm{m}^{-1}$ [36]. We assumed no X-ray refraction inside the alveolus cavity.

Figure 6a, c show simulated phase-contrast images at 30 and 50 cm detector–specimen distance. The image processing method was applied to these images to identify the tumor boundaries, and the results are shown by Fig. 6b, d.

Finally, we tackled the issue of motion in live specimens: this constitutes a major problem in the detection of small tumors. Indeed, without suitable fast image taking, motion blurring can make minute details impossible to observe. The effects of motion blurring are visible in Fig. 7 by two consecutive images in a movie sequence. The micrographs were separated by 0.1 s, and the image taking time was 1 ms. The details are sharper in Fig. 7b, whereas faster motion produces stronger edge blurring in Fig. 7a.

This indicates that a 1-ms image taking time is not necessarily short enough to completely "freeze" the cardiac and breathing motions and obtain sharp images. Thus, a spatially coherent X-ray source is not sufficient to obtain sharp images by phase contrast: the image taking time must also be suitably shortened by optimizing experimental conditions such as the geometry and the X-ray flux.

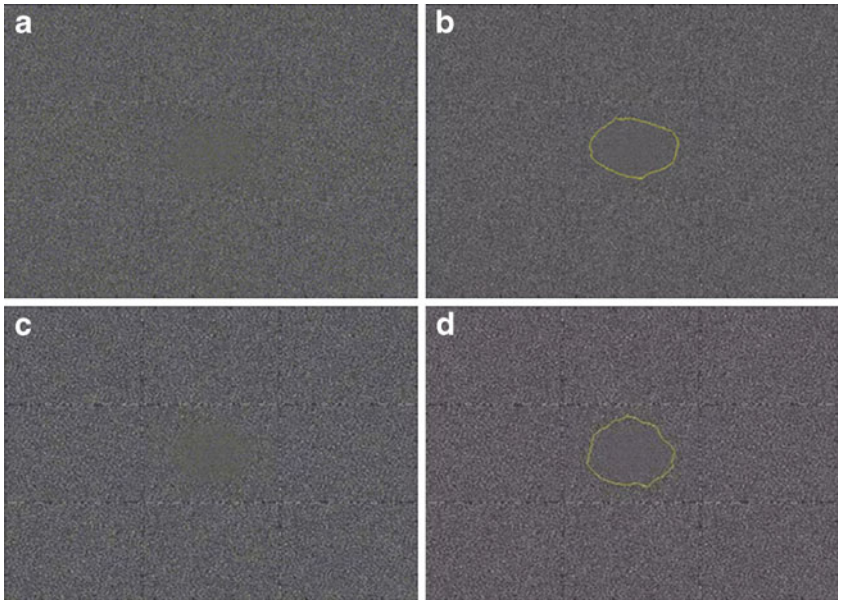

Fig. 6 (**a**, **c**) Simulated phase contrast radiographs of a human lung tumor for two different specimen–detector distances, 30 and 50 cm. (**b**, **d**) Corresponding results of the automatic tracing of the cancer boundaries

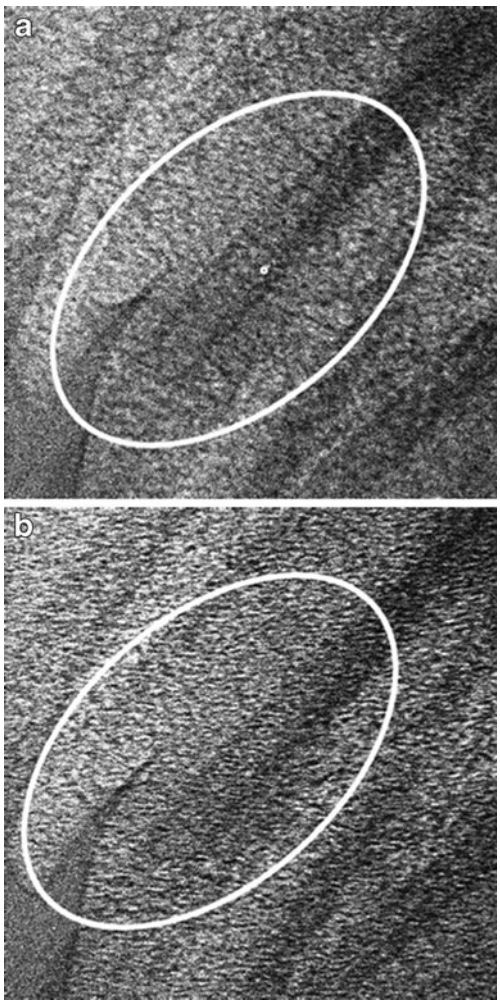

Fig. 7 Two sequential phase-contrast X-ray micrographs of a mouse lung cancer area from a movie. The time per image was 1 ms, and the two pictures were separated by 100 ms. The breathing and heartbeat produced motion blurring, more marked in (**a**) than in (**b**). Field of view, 3× 3 mm^2; the *ellipses* mark the same area, emphasizing the motion

Overall, the results presented in this article show that phase contrast can be exploited to detect and analyze small tumors and inflammation areas in lungs. Their impact, however, could be weakened by the need to use large, centralized synchrotrons to obtain coherent X-rays. Conversely, it could be enhanced if one could use laboratory-based sources. The current technological evolution is quite encouraging in that regard: high spatial coherence can be obtained with relatively small devices such as microfocused [37], laser plasma [38, 39], table-top synchrotron [40], or inverse-Compton [41, 42] sources. We performed preliminary tests on a sacrificed mouse with a microfocused source (Hamamatsu, L9191) obtaining positive results: the <10-μm source size was sufficient to reveal small details in the mouse lung structure.

On the other hand, motion blurring is still a problem with small-size sources [43]. To detect and analyze a millimeter-size tumor, the blurring cannot exceed a few tens of a micrometer. This corresponds to a time per image below 1 ms for the mouse cardiac motion. Ongoing developments, in particular those concerning laser plasma sources, compact synchrotrons, and inverse Compton scattering sources, could satisfy this requirement. Furthermore, the problems could be solved in part by synchronizing the radiograph taking with electrocardiography.

Conclusion

We demonstrated that refractive index radiology already reaches the required performances to detect submillimeter-size lung cancer tumors in live mice and to distinguish them from inflamed areas. Among the different types of tumors, phase-contrast radiology is particularly suitable for lung

cancer because of the large difference in the X-ray refractive index between air (in pulmonary alveoli) and the surrounding normal, cancer, and inflammatory tissues. Post-acquisition image processing was able to detect the differences, to mark accurately the location of tumors and to further enhance the detection sensitivity. Additional developments concerning in particular high-brilliance effective compact X-ray sources and high-efficiency detectors are required to sufficiently reduce the radiation dose and the motion blur so that clinical applications can be considered.

Acknowledgements We thank Ms. Yijing Guan for computer processing and Dr. Cyril Petibois for fruitful discussion. This work was supported by NNSF of 11079049 (China) and by CAS of KJCX3, SYW.N3 (China), NPST for Nanoscience and Nanotechnology, Thematic Program of Academia Sinica, the Biomedical NanoImaging Core Facility(Taiwan), Fonds National Suisse, Lausanne Center for Biomedical Imaging (CIBM), and the Creative Research Initiatives (Functional X-ray Imaging) of MOST/KOSEF (Korea).

References

1. Baldwin DR (2011) Imaging in lung cancer: recent advances in PET-CT and screening. Thorax 66:275–277
2. Van't Westeinde SC, van Klaveren RJ (2011) Screening and early detection of lung cancer. Cancer J 17:3–10
3. Henschke CI, Yankelevitz DF, Libby DM, Pasmantier MW, Smith JP, Miettinen OS (2006) Survival of patients with stage I lung cancer detected on CT screening. N Engl J Med 355:1763–1771
4. Bach PB, Jett JR, Pastorino U, Tockman MS, Swensen SJ, Begg CB (2007) Computed tomography screening and lung cancer outcomes. Jama 297:953–961
5. Liang EY, Chan M, Hsiang JH, Walkden SB, Poon WS, Lam WW, Metreweli C (1995) Detection and assessment of intracranial aneurysms: value of CT angiography with shaded-surface display. AJR Am J Roentgenol 165:1497–1502
6. Jankowski A, Martinelli T, Timsit JF, Brambilla C, Thony F, Coulomb M, Ferretti G (2007) Pulmonary nodule detection on MDCT images: evaluation of diagnostic performance using thin axial images, maximum intensity projections, and computer-assisted detection. Eur Radiol 17:3148–3156
7. Mulshine JL, Sullivan DC (2005) Clinical practice. Lung cancer screening. N Engl J Med 352:2714–2720
8. Swensen SJ, Jett JR, Hartman TE, Midthun DE, Mandrekar SJ, Hillman SL, Sykes AM, Aughenbaugh GL, Bungum AO, Allen KL (2005) CT screening for lung cancer: five-year prospective experience. Radiology 235:259–265
9. Markowitz SB, Miller A, Miller J, Manowitz A, Kieding S, Sider L, Morabia A (2007) Ability of low-dose helical CT to distinguish between benign and malignant noncalcified lung nodules. Chest 131:1028–1034
10. Haberkorn U, Schoenberg SO (2001) Imaging of lung cancer with CT, MRT and PET. Lung Cancer 34(Suppl 3):S13–S23
11. Yi CA, Jeon TY, Lee KS, Lee JH, Seo JB, Kim YK, Chung MJ (2007) 3-T MRI: usefulness for evaluating primary lung cancer and small nodules in lobes not containing primary tumors. Am J Roentgenol 189(2):386–392
12. Ung YC, Maziak DE, Vanderveen JA, Smith CA, Gulenchyn K, Lacchetti C, Evans WK (2007) 18Fluorodeoxyglucose positron emission tomography in the diagnosis and staging of lung cancer: a systematic review. J Natl Cancer Inst 99:1753–1767
13. Greco C, Rosenzweig K, Cascini GL, Tamburrini O (2007) Current status of PET/CT for tumour volume definition in radiotherapy treatment planning for non-small cell lung cancer (NSCLC). Lung Cancer 57:125–134
14. Meuli R, Hwu Y, Je JH, Margaritondo G (2004) Synchrotron radiation in radiology: radiology techniques based on synchrotron sources. Eur Radiol 14:1550–1560
15. Hwu Y, Tsai W-L, Groso A, Margaritondo G, Je JH (2002) Coherence-enhanced synchrotron radiology: simple theory and practical applications. J Phys D Appl Phys 35:R105–R120
16. Castelli E, Arfelli F, Dreossi D, Longo R, Rokvic T, Cova MA, Quaia E, Tonutti M, Zanconati F, Abrami A, Chenda V, Menk RH, Quai E, Tromba G, Bregant P, de Guarrini F (2007) Clinical mammography at the SYRMEP beam line. Nucl Instr Meth Phys Res A 572:237–240
17. Elleaume H, Fiedler S, Esteve F, Bertrand B, Charvet AM, Berkvens P, Berruyer G, Brochard T, Le Duc G, Nemoz C, Renier M, Suortti P, Thomlinson W, Le Bas JF (2000) First human transvenous coronary angiography at the European Synchrotron Radiation Facility. Phys Med Biol 45:L39–L43
18. Dix WR, Kupper W, Dill T, Hamm CW, Job H, Lohmann M, Reime B, Ventura R (2003) Comparison of intravenous coronary angiography using synchrotron radiation with selective coronary angiography. J Synchrotron Radiat 10:219–227
19. Dreossi D, Abrami A, Arfelli F, Bregant P, Casarin K, Chenda V, Cova MA, Longo R, Menk RH, Quai E, Quaia E, Rigon L, Rokvic T, Sanabor D, Tonutti M, Tromba G, Vascotto A, Zanconati F, Castelli E (2008) The mammography project at the SYRMEP beamline. Eur J Radiol 68:S58–S62
20. Fiedler S, Bravin A, Keyrilainen J, Fernandez M, Suortti P, Thomlinson W, Tenhunen M, Virkkunen P, Karjalainen-Lindsberg M (2004) Imaging lobular breast carcinoma: comparison of synchrotron radiation DEI-CT technique with clinical CT, mammography and histology. Phys Med Biol 49:175–188
21. Hooper SB, Kitchen MJ, Siew ML, Lewis RA, Fouras A, te Pas AB, Siu KK, Yagi N, Uesugi K, Wallace MJ (2009) Imaging lung aeration and lung liquid clearance at birth using phase contrast X-ray imaging. Clin Exp Pharmacol Physiol 36:117–125
22. Zhang L, Li D, Luo S (2011) Non-invasive microstructure and morphology investigation of the mouse lung: qualitative description and quantitative measurement. PLoS ONE 6:e17400
23. Liu P, Sun J, Guan Y, Yue W, Xu LX, Li Y, Zhang G, Hwu Y, Je JH, Margaritondo G (2008) Morphological study of early-stage lung cancer using synchrotron radiation. J Synchrotron Radiat 15:36–42
24. Hwu Y, Tsai WL, Chang HM, Yeh HI, Hsu PC, Yang YC, Su YT, Tsai HL, Chow GM, Ho PC, Li SC, Moser HO, Yang P, Seol SK, Kim CC, Je JH, Stefanekova E, Groso A, Margaritondo G (2004) Imaging cells and tissues with refractive index radiology. Biophys J 87:4180–4187
25. Song YF, Chang CH, Liu CY, Chang SH, Jeng US, Lai YH, Liu DG, Chung SC, Tsang KL, Yin GC, Lee JF, Sheu HS, Tang MT, Hwang CS, Hwu YK, Liang KS (2007) X-ray beamlines for structural studies at the NSRRC superconducting wavelength shifter. J Synchrotron Radiat 14:320–325
26. Baik S, Kim HS, Jeong MH, Lee CS, Je JH, Hwu Y, Margaritondo G (2004) International consortium on phase contrast imaging and radiology beamline at the Pohang Light Source. Rev Sci Instrum 75:4355–4358
27. Margaritondo G, Hwu Y, Je JH (2004) Synchrotron light in medical and materials science radiology. Riv Nuovo Cimento 27:1–40
28. Hwu Y, Je JH, Margaritondo G (2005) Real-time radiology in the microscale. Nucl Instrum Meth A 551:108–118
29. Hamide JP, Qian Z, Xu H, Diethelm L, Skrepnik N, Castaneda-Zuniga WR, Hunt JD (1997) Percutaneous implantation of non-

small-cell lung carcinoma: technique and observations. Acad Radiol 4:629–633
30. Tong Y, Zhang G, Li Y, Tan M, Wang W, Chen J, Hwu Y, Hsu PC, Je JH, Margaritondo G, Song W, Jiang R, Jiang Z (2006) Synchrotron microradiography study on acute lung injury of mouse caused by PM(2.5) aerosols. Eur J Radiol 58:266–272
31. Yue W, Zhang G, Liu P, Sun J, Yeukuang H, Je JH, Tan M, Li Y (2007) Aerosol-induced lung injuries observed by synchrotron radiation X-ray phase-contrast imaging technique, vol. 262, no. 2. Elsevier, Amsterdam, PAYS-BAS
32. Su WY, Jaskot RH, Richards J, Abramson SR, Woessner JF Jr, Yu WH, Dreher KL (2000) Induction of pulmonary matrilysin expression by combustion and ambient air particles. Am J Physiol Lung Cell Mol Physiol 279:L152–L160
33. Canny J (1986) A computational approach to edge detection. Pattern analysis and machine intelligence. IEEE Trans PAMI 8:679–698
34. Xu C, Prince JL (1998) Snakes, shapes, and gradient vector flow. IEEE Trans Image Process 7:359–369
35. Kass M, Witkin A, Terzopoulos D (1988) Snakes: active contour models. Int J Comput Vision 1:321–331
36. Kitchen MJ, Paganin D, Lewis RA, Yagi N, Uesugi K, Mudie ST (2004) On the origin of speckle in x-ray phase contrast images of lung tissue. Phys Med Biol 49:4335–4348
37. Tuohimaa T, Otendal M, Hertz HM (2007) Phase-contrast x-ray imaging with a liquid-metal-jet-anode microfocus source. Appl Phys Lett 91:074104
38. Lazzaro PD, Bollanti S, Conti A, Flora F, Mezi L, Murra D, Zheng CE (2005) Recent results of laser-driven EUV and soft X-rays plasma source at ENEA Frascati. Proc SPIE 5958:595814
39. Krol A, Ikhlef A, Kieffer JC, Bassano DA, Chamberlain CC, Jiang Z, Pepin H, Prasad SC (1997) Laser-based microfocused x-ray source for mammography: feasibility study. Med Phys 24:725–732
40. Yamada H (2003) Novel X-ray source based on a tabletop synchrotron and its unique features. Nucl Instrum Methods Phys Res B 199:509–516
41. Zheng D, Frederick WJ, DeStefano C, Vlieks AE, Landahl E, Kwan A, Heritage JP, Norman A, Boone JM, Luhmann NC (2006) The monochromatic Compton X-ray source for cancer diagnostics and therapy. Infrared Millimeter Waves and 14th International Conference on Teraherz Electronics, pp 580–580
42. Vlieks AE, Akre R, Caryotakis G, Destefano C, Frederick WJ, Heritage JP, Luhmann NC, Martin D, Pellegrini C (2006) Recent measurements and plans for the SLAC Compton X-ray source. AIP Conf Proc 807:481–490
43. Hwu Y, Tsai WL, Je JH, Seol SK, Kim B, Groso A, Margaritondo G, Lee KH, Seong JK (2004) Synchrotron microangiography with no contrast agent. Phys Med Biol 49:501–508